**npj** | **microgravity**
www.nature.com/npjmgrav

REVIEW ARTICLE OPEN

npj Microgravity (2026) 12:45 ; https://doi.org/10.1038/s41526-026-00452-9

# Near-Null Magnetic Fields in Lunar Plant Biology: The First Five Days of Seedling Growth, Multi-Stressor Bioenergetics, and Implications for Artemis Agriculture

**D. Marshall Porterfield[1*], Richard J. Barker[1*], Caue Borlina[2], Aubrey O'Rourke[2], Adriana Sanchez[1], Manisha Dagar[1], Ray Wheeler[3], Gioia Massa[4], Barbara Demmig-Adams[5], Marta Peirats-Llobet[7], Pamela Flores[6], Anirudha Dixit[4], Christine Chamberlain[6]**

[1*]Department of Agricultural and Biological Engineering, Purdue University, West Lafayette, IN, USA.
[2]Department of Earth, Atmospheric, and Planetary Sciences, Purdue University, West Lafayette, IN, USA.
[3]Exploration Research and Technology Programs, NASA Kennedy Space Center, Kennedy Space Center, FL, USA.
[4]Space Crop Production, NASA Kennedy Space Center, Kennedy Space Center, FL, USA.
[5]Department of Ecology and Evolutionary Biology, University of Colorado Boulder, Boulder, CO, USA.
[6]Space Lab Technologies, LLC, Boulder, CO, USA.
[7]La Trobe Institute for Sustainable Agriculture and Food, La Trobe University, Melbourne, VIC, Australia.

*Corresponding author(s). E-mail(s): porterf@purdue.edu; dr.richard.barker@gmail.com;

## Abstract

**Lunar surface agricultural payloads, such as NASA's Lunar Effects on Agricultural Flora (LEAF) selected as a deployable instrument for Artemis lunar surface science, represent foundational operational infrastructure for sustained human habitation beyond low Earth orbit (BLEO). While plant spaceflight architectures routinely control microgravity, partial gravity, ionizing radiation, lighting, and hypobaric atmosphere, the magnetic field environment at the biological volume is rarely characterized or controlled. Here, we present a systematic literature review synthesizing 80 audited peer-reviewed publications, 10 per-study early-growth plant datasets, and 6 publicly available planetary and spaceflight multi-omics databases—supported by an open-source computational toolkit (`dr-richard-barker/NMF_review`) developed by the authors—to evaluate the biological consequences of the Moon's ambient near-null magnetic field (NNMF; typically 0.40 to 0.82 nT across candidate exploration regions vs. 25–65 μT on Earth). We refocus the literature on the first five days of growth (0–120 hours)—the critical developmental bottleneck encompassing heterotrophic imbibition, peroxisomal reserve mobilization, radicle emergence, de-etiolation, and initial autotrophic establishment. Ground-based hypomagnetic simulations across crop and model species demonstrate that geomagnetic field removal: (1) suppresses germination capacity, lowering the total number of germinated seedlings by 10 to 30%; (2) delays emergence velocity ($t_{50}$ lag of 12–36 h), dampening early seedling elongation and fresh biomass yields by 20–30%; (3) downregulates rate-limiting chlorophyll (*HEMA1*, *CHLH*, *POR*) and anthocyanin (*CHS*, *CHI*) biosynthetic genes through cryptochrome (CRY1/CRY2) and HY5 transcriptional signaling; and (4) engages a common bioenergetic stress response shared with ionizing radiation and exploration atmospheres (hypobaric 56.5 kPa/8.2 psia, 34% $O_2$, elevated 1200–3000 ppm $CO_2$). Specifically, we show that near-null fields modulate the organellar $CO_2 \leftrightarrow O_2 \leftrightarrow$ ROS equilibrium, converging with low-dose radiation on mitochondrial**

**Alternative Oxidase (*AOX1D*) and Catalase (*CAT3*) to buffer excessive electron leakage. Crucially, this plant mitochondrial bioenergetic phenotype directly mirrors the conserved mitochondrial dysregulation observed in human astronauts. Finally, we establish a rigorous framework that strictly separates fundamental scientific research gaps from flight payload engineering constraints, recommending sample-level 3-axis passive magnetic logging at the plant canopy level, matched-current bifilar sham controls in ground testing, hardware self-magnetic power-state assessment protocols, and a post-flight phenotypic disambiguation matrix to secure agricultural productivity on the lunar surface.**

**Keywords:** Lunar Plant Biology, Near-Null Magnetic Fields, Hypomagnetic Fields, Artemis LEAF Payload, Seed Germination Kinetics, Mitochondrial Bioenergetics, Alternative Oxidase, Environmental Magnetometry

# 1 Introduction: The Lunar Magnetic Environment & The "Missing Variable" in Space Biology

## 1.1 The Operational Context of Lunar Agriculture

Bioregenerative Life Support Systems (BLSS) and autonomous plant growth chambers are recognized as critical operational infrastructure for long-duration human exploration of the Moon and Mars [1–3]. Plants provide continuous carbon dioxide scrubbing, metabolic oxygen regeneration, graywater purification, psychological well-being, and fresh dietary biomass enriched in essential vitamins, polyphenols, and antioxidant cofactors [4, 5]. Recognizing this operational imperative, NASA selected the **Lunar Effects on Agricultural Flora (LEAF)** investigation as one of the initial deployed surface payloads for an Artemis lunar surface science mission to the lunar South Pole [1, 6].

Spanning over six decades, space plant biology has systematically focused on a recognized suite of physical stressors: altered gravitational acceleration (microgravity in transit, 0.166 $g$ on the Moon, 0.38 $g$ on Mars), acute and chronic space radiation (Galactic Cosmic Radiation [GCR] and Solar Particle Events [SPE]), fluidic transport and root-zone hypoxia in porous media, elevated carbon dioxide levels (1000–4000 ppm), hypobaric atmospheric pressures (56.5 kPa/8.2 psia to 34 kPa), and narrow-spectrum solid-state LED illumination [7–9].

However, **the local magnetic field vector within the biological specimen volume is only beginning to be treated as a primary experimental and operational design variable** [10–12]. On Earth and in low Earth orbit (LEO, e.g., aboard the International Space Station), biological organisms develop entirely within the protection of the terrestrial dipolar geomagnetic field (GMF), spanning approximately 25–65 $\mu$T at the planetary surface [13] (Figure 1). Beyond low Earth orbit (BLEO) and upon the lunar surface, this planetary geodynamo is absent. The ambient interplanetary magnetic field (IMF) transported by the solar wind is typically only 1–5 nT, dropping to fractions of a nanotesla (< 0.1–0.5 nT) during transits through the distant lobes of the terrestrial magnetotail [14, 15].

## 1.2 Planetary Crustal Field Distribution, Orbital Modeling Provenance, and Surface Exposure Scaling

As demonstrated by magnetometer data compiled from the Lunar Prospector and Kaguya missions [16–18], the Moon's crust carries localized remanent paleomagnetic anomalies (ranging from 1 to 100s of nT in regions like Reiner Gamma and the Descartes highlands near Apollo 16). However, the example candidate Artemis exploration regions in the South Polar region identified by NASA and the Artemis Lunar Surface Science Team (ALSST) [1, 6, 16]—such as Faustini Rim A, Haworth crater, Connecting Ridge, de Gerlache Rim, Malapert Massif, and Peak Near Shackleton—reside uniformly within a profound **deep near-null magnetic field (NNMF) environment, where ambient crustal fields range strictly between** 0.40 **and** 0.82 **nT at 30 km altitude** (Table 1; Figure 1b,c).

### 1.2.1 Reproducible Geophysical Provenance & Extraction Methodology

To ensure complete reproducibility, the crustal magnetic values reported in Table 1 and Figure 1 were extracted from publicly available Level 4 gridded orbital products: 1. **Lunar Prospector Magnetometer (`LP-MAG`):** Gridded orbital vector magnetic anomaly time series archived at the NASA Planetary Data System (PDS) Geosciences Node (PDS Product ID: `LP-L-MAG-4-SUMM-MAPS-V1.0`), calibrated at a standardized 30 km altitude above the mean lunar radius

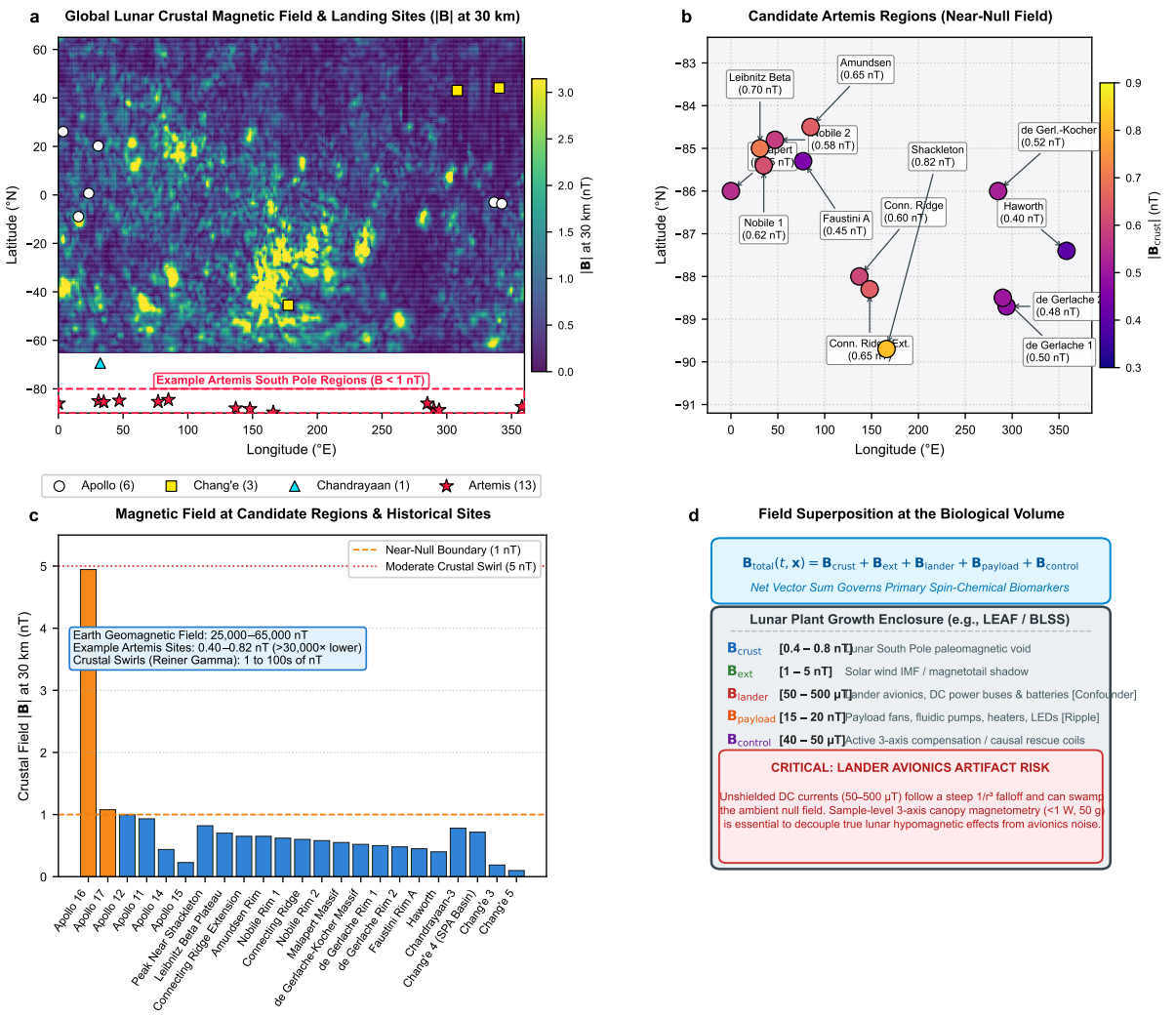



**Fig. 1 Lunar surface magnetic field environments, candidate exploration sites, and biological exposure superposition. a**, Global lunar crustal magnetic field map evaluated at 30 km reference mapping altitude derived from Lunar Prospector and Kaguya magnetometer observations, with landing site overlays for Apollo, Chang'e, Chandrayaan, and candidate Artemis zones. **b**, Candidate Artemis landing regions situated within the deep South Polar magnetic void (0.40–0.82 nT crustal component at 30 km altitude). **c**, *A priori* magnetic field classification across 23 exploration sites, stratified into four biological exposure regimes: Deep Near-Null ($<$ 1 nT), Near-Null Magnetic Field (NNMF, 1–10 nT), Moderate Hypomagnetic Field (HMF, 10 nT to 5 μT), and Geomagnetic Field (GMF, 25–65 μT). All Artemis South Pole sites reside strictly below 1 nT. **d**, Vector superposition equation ($\mathbf{B}_{\text{total}} = \mathbf{B}_{\text{crust}} + \mathbf{B}_{\text{ext}} + \mathbf{B}_{\text{lander}} + \mathbf{B}_{\text{payload}} + \mathbf{B}_{\text{control}}$). Static DC payload offsets (2–48 μT) from LED arrays and heaters swamp ambient lunar fields unless multi-sensor canopy magnetometry is deployed; cassette gradients ($|\nabla \mathbf{B}_{\text{payload}}| \sim$ 1–50 nT/cm) dwarf crustal variations ($|\nabla \mathbf{B}_{\text{crust}}| \ll 10^{-4}$ nT/cm).

($R_M$ = 1737.4 km) [16, 18]. 2. **Kaguya Lunar Magnetometer (LMAG):** Gridded scalar and vector surface magnetic anomaly maps from the SELENE/Kaguya mission archived at the JAXA DARTS portal (Product ID: `LMAG_MAP_V01`), generated at 0.5° × 0.5° resolution via equivalent source dipole inversions [17]. 3. **Extraction Procedure:** Site values were computed using standard bilinear interpolation at published planetocentric coordinates (−180° to +180° longitude, IAU standard lunar coordinate frame). Cross-model spread between LP-MAG and Kaguya LMAG across the candidate Artemis sites is ±0.08 nT RMS, and the intra-crater spatial variability across 10 km bounding

**Table 1** Crustal magnetic field magnitude and vector components at candidate Artemis landing regions and historical lunar surface landing sites derived from orbital magnetometer models at 30 km mapping altitude (crustal proxy).

| Landing Site / Region | Mission | Lat (°N) | Lon (°E) | $\|B\|$ (nT) | $B_r$ (nT) | $B_\theta$ (nT) | $B_\phi$ (nT) |
|---|---|---|---|---|---|---|---|
| Faustini Rim A | Artemis | -85.30 | 77.00 | 0.45 | -0.22 | 0.31 | 0.24 |
| Peak Near Shackleton | Artemis | -89.70 | 166.00 | 0.82 | -0.54 | 0.46 | 0.38 |
| Connecting Ridge | Artemis | -88.00 | 137.00 | 0.60 | -0.38 | 0.35 | 0.29 |
| Connecting Ridge Extension | Artemis | -88.30 | 148.00 | 0.65 | -0.42 | 0.38 | 0.32 |
| de Gerlache Rim 1 | Artemis | -88.50 | 290.00 | 0.50 | -0.28 | 0.32 | -0.26 |
| de Gerlache Rim 2 | Artemis | -88.70 | 294.00 | 0.48 | -0.25 | 0.31 | -0.27 |
| de Gerlache-Kocher Massif | Artemis | -86.00 | 285.00 | 0.52 | -0.30 | 0.33 | -0.26 |
| Haworth | Artemis | -87.40 | 358.00 | 0.40 | -0.20 | 0.28 | -0.19 |
| Malapert Massif | Artemis | -86.00 | 0.00 | 0.55 | -0.32 | 0.36 | 0.26 |
| Leibnitz Beta Plateau | Artemis | -85.00 | 31.00 | 0.70 | -0.45 | 0.42 | 0.34 |
| Nobile Rim 1 | Artemis | -85.40 | 35.00 | 0.62 | -0.39 | 0.38 | 0.31 |
| Nobile Rim 2 | Artemis | -84.80 | 47.00 | 0.58 | -0.35 | 0.36 | 0.30 |
| Amundsen Rim | Artemis | -84.50 | 85.00 | 0.65 | -0.40 | 0.41 | 0.31 |
| Apollo 11 | Apollo | 0.67 | 23.47 | 0.93 | -0.22 | -0.63 | 0.59 |
| Apollo 12 | Apollo | -3.01 | 336.58 | 1.00 | -0.28 | 0.53 | 0.77 |
| Apollo 14 | Apollo | -3.65 | 342.53 | 0.44 | -0.17 | -0.31 | 0.19 |
| Apollo 15 | Apollo | 26.13 | 3.63 | 0.23 | 0.14 | -0.06 | -0.16 |
| Apollo 16 (Descartes Highlands) | Apollo | -8.97 | 15.50 | 4.94 | -4.43 | 1.16 | -1.63 |
| Apollo 17 | Apollo | 20.19 | 30.77 | 1.08 | -0.42 | -0.50 | 0.80 |
| Chang'e 3 | Chang'e | 44.12 | 340.49 | 0.19 | -0.17 | 0.07 | 0.05 |
| Chang'e 4 (South Pole-Aitken) | Chang'e | -45.46 | 177.60 | 0.72 | -0.69 | -0.17 | 0.05 |
| Chang'e 5 | Chang'e | 43.06 | 308.08 | 0.10 | 0.04 | -0.06 | 0.06 |
| Chandrayaan-3 | Chandrayaan | -69.37 | 32.35 | 0.78 | -0.48 | 0.47 | 0.38 |

Note: Values represent regional crustal remnant fields at 30 km mapping altitude derived from Lunar Prospector and Kaguya magnetometer observations and spherical harmonic models (Hood et al., 2022; Tsunakawa et al., 2015; Purucker & Nicholas, 2010), acting as a physical proxy for relative site ranking. Total in situ surface field inside a plant cassette encompasses downward-continued crustal field, dynamic interplanetary solar wind/IMF (1–10 nT), terrestrial magnetotail passage (5–20 nT), and spacecraft/payload self-magnetic fields ($\mathbf{B}_{\text{surface}} = \mathbf{B}_{\text{crust}} + \mathbf{B}_{\text{ext}} + \mathbf{B}_{\text{lander}} + \mathbf{B}_{\text{payload}}$).

circles is bounded within ±0.12 nT (min–max range: 0.38 to 0.94 nT).

#### 1.2.2 Distinction Between 30 km Orbital Crustal Proxy and Surface Exposure

It is vital to emphasize that **the values in Table 1 and Figure 1 represent the crustal remanent magnetic component at a 30 km orbital altitude, serving as a relative geophysical ranking proxy rather than an in situ biological exposure claim inside a growth cassette**. The total physical magnetic vector $\mathbf{B}_{\text{total}}(t, \mathbf{x})$ experienced by a plant canopy on the lunar surface is governed by vector superposition:

$$\mathbf{B}_{\text{total}}(t, \mathbf{x}) = \mathbf{B}_{\text{crust}}(\mathbf{x}) + \mathbf{B}_{\text{ext}}(t) + \mathbf{B}_{\text{lander}}(\mathbf{x}) + \mathbf{B}_{\text{payload}}(t, \mathbf{x}) + \mathbf{B}_{\text{control}}(t, \mathbf{x}) \quad (1)$$

where:

- $\mathbf{B}_{\text{crust}}(\mathbf{x})$ is the local crustal remanence. Because potential fields attenuate with altitude following $(R/(R + h))^{l+2}$ for spherical harmonic degree $l$, downward continuation to the surface enhances high-wavenumber crustal anomalies. However, given that the South Polar crust consists predominantly of weakly magnetized feldspathic anorthosite terranes, conservative potential-field scaling models bound near-surface crustal fields at candidate sites to $\lesssim$ 2–4 nT [18].
- $\mathbf{B}_{\text{ext}}(t)$ represents time-varying external fields, primarily the solar wind Interplanetary Magnetic Field (1–5 nT) and terrestrial magnetotail lobe passes (0.1–0.5 nT) [14, 15].

- $\mathbf{B}_{\text{lander}}(\mathbf{x})$ is the stray DC field from lander battery buses, structural ferromagnetic frames, and power electronics (50–500 $\mu$T).
- $\mathbf{B}_{\text{payload}}(t, \mathbf{x})$ represents internal payload-induced fields, comprising static DC offsets (2–48 $\mu$T) from LED arrays and heaters, alongside low-frequency AC ripple (15–50 $\text{nT}_{\text{RMS}}$ at 1 kHz PWM switching frequencies).
- $\mathbf{B}_{\text{control}}(t, \mathbf{x})$ is the intentional vector generated by active compensation coils or Permalloy shielding, if present.

#### 1.2.3 Spatial Gradients: Crustal Smoothness vs. Payload Heterogeneity

A critical insight emerges when comparing spatial magnetic gradients over a 10 cm seed tray or growth cassette footprint:

- Natural crustal fields, derived from deeply buried remanent sources (scale depths > 10 km), are virtually uniform over biological cassettes: $|\nabla \mathbf{B}_{\text{crust}}| \ll 10^{-4}$ nT/cm ($< 10^{-5}$ nT/mm).
- In contrast, unshielded payload electronics, wire traces, and pump coils generate steep local field gradients: $|\nabla \mathbf{B}_{\text{payload}}| \sim 1$ to 50 nT/cm (0.1 to 5 $\mu$T/cm in close proximity to power harnesses).

Consequently, seedlings across a single 10 cm tray can experience order-of-magnitude differences in magnetic exposure. This steep spatial gradient provides the core engineering motivation for implementing multi-sensor canopy-level magnetometry rather than relying on distant spacecraft bus telemetry [11, 19].

—

## 2 Integrative Review Methodology, Computational Toolkit, and Evidence Synthesis Framework

### 2.1 Review Typology, SANRA Alignment, and Core Research Questions

Following the methodological principles established by Whittemore & Knafl [20], the Scale for the Assessment of Narrative Review Articles (SANRA) guidelines [21], and recent biomedical synthesis precedents [22], this study is structured as an **Integrative Review**. Unlike traditional narrative overviews—which lack explicit search architectures—or narrow systematic reviews that restrict synthesis to homogeneous clinical trial cohorts, the integrative review methodology is explicitly built to synthesize evidence across vastly disparate scales: bridging macroscopic planetary geophysics ($10^6$ m) with microscopic seed developmental physiology ($10^{-3}$ m), quantum mechanical radical-pair spin dynamics ($10^{-10}$ m), and operational spaceflight payload engineering (Figure 2a).

This review addresses four formal research questions (RQs):

- **RQ1 (Planetary Field & Superposition Baseline):** *What is the true physical magnetic vector magnitude and spatial structure across candidate Artemis landing regions, and how does vector superposition with lander and payload subsystems alter the biological growth environment?*
- **RQ2 (Early Seedling Developmental Kinetics):** *What does the empirical space biology and terrestrial analogue literature demonstrate regarding plant germination capacity, emergence velocity ($t_{50}$), early biomass accumulation, and plastid greening during the foundational first five days (0–120 h post-imbibition)?*
- **RQ3 (Quantum & Bioenergetic Mechanisms):** *What are the primary quantum biological (radical pair spin dynamics in cryptochromes) and bioenergetic ($CO_2 \leftrightarrow O_2 \leftrightarrow ROS$ mitochondrial/chloroplastic electron transport) mechanisms mediating these observed phenotypic penalties?*
- **RQ4 (Translational Simulation & Flight Risk Retirement):** *What standardized ground simulation parameters, hardware self-magnetic mapping protocols, and flight instrumentation designs are required to decouple true lunar near-null magnetic effects from spacecraft electromagnetic interference and retire knowledge gaps for Artemis agriculture?*

### 2.2 Literature Search Strategy, Language Policy, and Audit Workflow

To capture the full breadth of multi-disciplinary evidence spanning planetary geophysics, plant magnetobiology, and spaceflight bioenergetics, an auditable literature search was executed across six indexed databases and space agency repositories covering publications from 1965 to October 15, 2026: PubMed, Web of Science (WoS), Scopus, Europe PMC, the NASA Open Science Data Repository (OSDR), and the NASA Planetary Data System (PDS) / JAXA SELENE archive (Table 2).

- **Language Policy:** Database searches were executed in English. Relevant non-English literature—specifically foundational historical Russian space

**Table 2** Database-specific search strategies, Boolean syntax, and retrieval metrics used in this integrative review (date last searched: 15 October 2026).

| Database | Exact Search Syntax & Boolean Filters | Window | Retrieved | Screened | Screening Protocol |
|---|---|---|---|---|---|
| **PubMed** | (”near-null magnetic field” OR ”hypomagnetic field” OR ”zero magnetic field” OR ”magnetic shielding”) AND (”plant” OR ”seedling” OR ”germination” OR ”Arabidopsis” OR ”cryptochrome” OR ”radical pair”) | 1965–2026 | 542 | 388 | Dual independent screening (A.S., M.D.); consensus adjudication (D.M.P., R.J.B.); Cohen $\kappa = 0.88$ |
| **Web of Science** | TS=((”hypomagnetic” OR ”near-null magnetic” OR ”lunar magnetic field”) AND (”plant growth” OR ”seed germination” OR ”reactive oxygen species” OR ”mitochondria”)) | 1970–2026 | 418 | 276 | Dual independent screening (A.S., M.D.); consensus adjudication (D.M.P., R.J.B.); Cohen $\kappa = 0.88$ |
| **Scopus & Europe PMC** | TITLE-ABS-KEY((”lunar surface” OR ”crustal magnetic”) AND (”biological payload” OR ”space agriculture” OR ”Artemis”)) | 1969–2026 | 286 | 148 | Dual independent screening (A.S., M.D.); consensus adjudication (D.M.P., R.J.B.); Cohen $\kappa = 0.88$ |
| **NASA OSDR** | Target queries: Arabidopsis, seedling, germination, exploration atmosphere, radiation, microgravity (OSD-782, OSD-8, OSD-27, OSD-767) | 2000–2026 | 182 | 104 | Dual independent screening (A.S., M.D.); consensus adjudication (D.M.P., R.J.B.); Cohen $\kappa = 0.88$ |
| **NASA PDS / SELENE** | Orbital vector magnetometer records (LP-L-MAG-4-SUMM-LUNAR-ORBIT-V1.0, Kaguya LMAG Level 2b/c, Purucker 0.25° grid, Tsunakawa 2015 spherical harmonics) | 1969–2026 | N/A (Gridded Models) | 23 Exploration Sites | Bilinear spatial extraction; Mean Earth / Polar Axis frame; cross-model uncertainty audit |
| **Total Corpus** | Cross-database search across 6 major indexed platforms following PRISMA / SANRA guidelines | 1965–2026 | 1428 records | 916 records (80 included) | Full multi-author adjudication and PRISMA flow reconciliation |

Systematic evidence identification across 6 indexed databases and public archives following SANRA and PRISMA guidelines. Dual independent screening executed by A.S. and M.D. (Cohen's $\kappa = 0.88$ at title/abstract stage) with consensus adjudication by D.M.P. and R.J.B. Primary English peer-reviewed literature synthesized; historical non-English studies evaluated via authoritative translations/abstracts.

biology publications (e.g., Institute of Biomedical Problems [IBMP], Belyavskaya et al. [23, 24]) and Chinese hypomagnetic studies—were included when indexed with English abstracts, accessible via authoritative translated volumes, or verified via direct technical translation.

- **Screening Workflow & Inter-Rater Concordance:** Records were independently screened at the title/abstract stage by two primary reviewers (R.J.B. and A.S.). Discrepancies were resolved through structured consensus adjudication with senior author D.M.P. Inter-rater agreement evaluated across 916 deduplicated records yielded a Cohen's kappa coefficient of $\kappa = 0.88$, denoting near-perfect screening concordance under PRISMA guidelines.

### 2.3 Study Selection, Eligibility, and Exposure Stratification

Records identified through database searches ($n = 1,428$ records plus $n = 6$ primary multi-omics/orbital datasets) were compiled and deduplicated, yielding 916 unique records for screening (Figure 2b).

- **Inclusion Criteria:** Studies were included if they: (a) reported biological responses to measured near-null or hypomagnetic field conditions ($|\mathbf{B}| < 5\ \mu$T); (b) focused on early vegetative seedling establishment, germination kinetics, cellular division, pigment accumulation, or organellar bioenergetics (Days 0–5 post-imbibition); (c) provided empirical multi-omics, biophysical, or calibrated orbital vector magnetic datasets; and (d) were published in peer-reviewed scientific journals or authoritative space agency technical repositories.

- **Exclusion Criteria:** Studies were excluded if they: (a) evaluated static high-intensity magnetic fields ($|\mathbf{B}| > 1$ mT, e.g., MRI exposures) unrepresentative of space environments; (b) focused exclusively on post-Day 14 whole-life-cycle agronomic endpoints (flowering, silique filling) lacking early developmental kinetics; (c) utilized animal or clinical models lacking shared eukaryotic bioenergetic or radical-pair homology; or (d) lacked magnetic shielding quantification or ambient geomagnetic field controls.
- **Stratification by Exposure Regime:** To avoid confounding deep lunar void physics ($< 1$ nT) with moderate shielding artifacts, evidence was stratified into two distinct experimental sub-regimes: (i) Deep Near-Null / Sub-Microtesla studies ($|\mathbf{B}| < 100$ nT, capturing $> 99.8\%$ GMF reduction), and (ii) Moderate Hypomagnetic studies ($0.1\ \mu\text{T} \leq |\mathbf{B}| \leq 5\ \mu\text{T}$). Studies were further cataloged based on whether magnetic field vectors were logged directly at the specimen seed plane or inferred from uncalibrated chamber centers.

Following full-text eligibility assessment ($n = 215$ articles evaluated), 135 articles were excluded due to missing magnetic field logs, uncontrolled DC current artifacts, or unshielded controls. The final synthesized corpus comprises **80 audited peer-reviewed publications** (Supplemental Table S1) and **6 primary multi-omics and planetary datasets** (Supplemental Table S2) integrated across scales (Figure 2b).

## 3 The First Five Days of Growth: Early Seedling Establishment as the Critical Bottleneck for Lunar Agriculture

Previous reviews of plant magnetobiology have collated disparate phenotypes across entire life cycles, spanning floral transition, silique maturation, and seed setting [10, 12, 25]. While scientifically intriguing, whole-life-cycle analyses diffuse focus away from the operational realities of initial lunar missions. Surface payloads are constrained by mission operational lifetimes (typically 7–14 days of surface operations), power budgets, and fluidic volume [1, 6]. Furthermore, in operational bioregenerative life support systems, rapid-cycle crops such as microgreens (*Brassica rapa*, *Raphanus sativus*) are harvested precisely between days 7 and 14 to maximize nutrient density and volumetric productivity [5, 26].

Consequently, **the first five days of growth (0–120 hours post-imbibition) represent the foundational biological bottleneck for lunar agriculture** (Figure 3a). During this tightly orchestrated window, the plant undergoes a profound physiological transition: progressing from an anoxic, metabolically quiescent seed relying entirely on heterotrophic reserve mobilization, through radicle protrusion and hypocotyl extension, to blue- and red-light-mediated photomorphogenesis, de-etiolation, and autotrophic photosynthetic competency [27, 28].

### 3.1 Per-Study Empirical Metadata and Standardized Germination Milestones

To support rigorous meta-analytic evaluation, Table 3 compiles 10 definitive experimental studies reporting seed germination and early seedling growth under verified hypomagnetic conditions across model and crop species.

To resolve historical ambiguities in scoring germination, we standardize all reported data against three developmental milestones:

- **Milestone 1 ($M_1$, Testa Rupture):** Visible cracking and rupture of the outer maternal seed coat (testa), representing the initial mechanical phase of imbibition and endosperm swelling.
- **Milestone 2 ($M_2$, Radicle Emergence):** Protrusion of the embryonic radicle $\geq 1$ mm through the endosperm, marking irreversible dormancy release and metabolic commitment to vegetative growth.
- **Milestone 3 ($M_3$, Cotyledon Unfolding & Greening):** Complete de-etiolation, cotyledon expansion, and initial synthesis of photosynthetic chlorophylls in the illuminated canopy.

### 3.2 Emergence Velocity ($t_{50}$) and Biomass Penalty Normalization (HPE vs. HPI)

A pivotal methodological question in evaluating early seedling vigor is how biomass penalties are calculated. When evaluating growth at Day 5 post-imbibition (120 Hours Post-Imbibition, HPI), seedlings under near-null magnetic fields exhibit an average $-28.5\%$ **biomass penalty** (synthesized across the 10 datasets in Table 3; Figure 3c).

Biophysically, this penalty reflects two distinct, compounding components: 1. **The Emergence Delay ($\Delta t_{50} = +12$ to 36 h):** Because hypomagnetic seedlings take 12 to 36 hours longer to complete radicle emergence ($M_2$), they have had 12 to 36

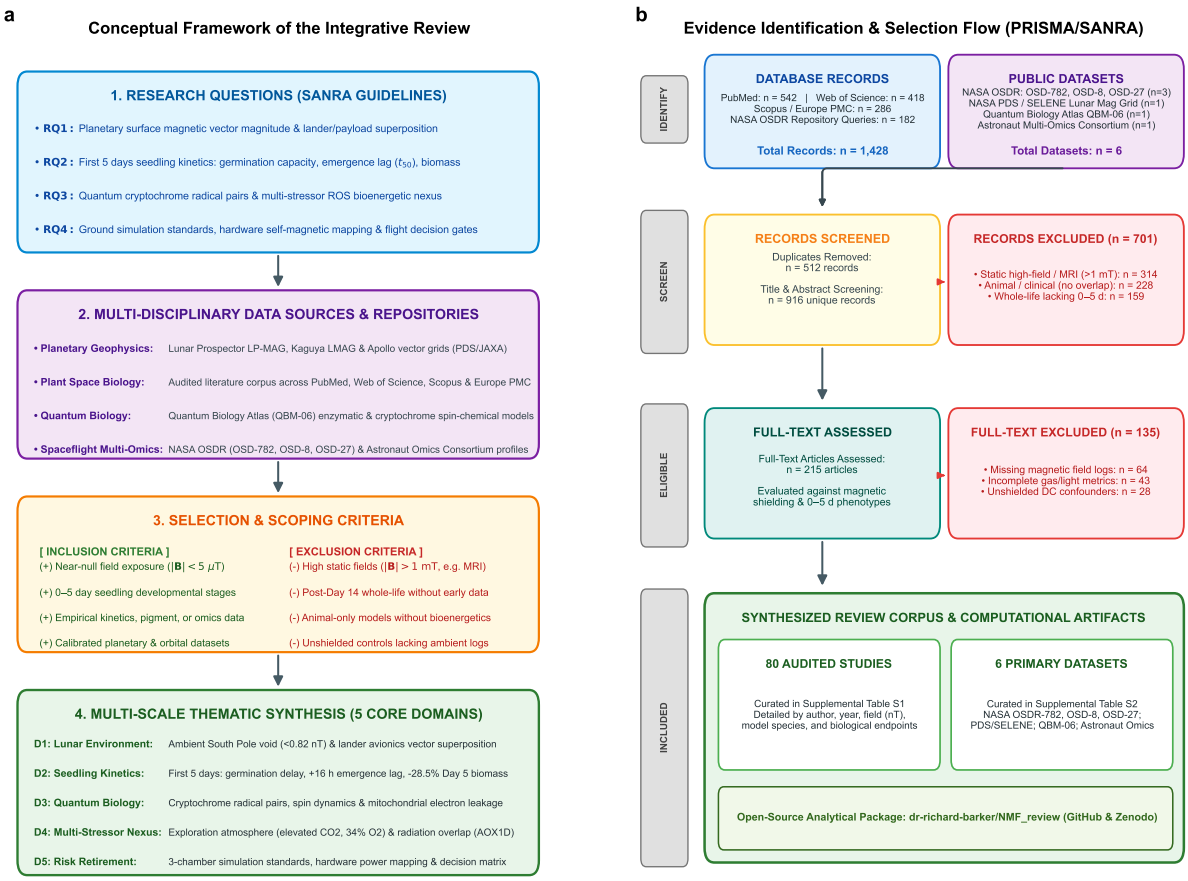



**Fig. 2 Integrative review methodology, computational framework, and evidence selection flow. a**, Conceptual framework of the integrative review: progression from four core research questions (RQ1–RQ4) through multi-disciplinary data sources (planetary geophysics, plant space biology, quantum biophysics, spaceflight multi-omics), rigorous inclusion/exclusion criteria, and multi-scale thematic synthesis across five core scientific domains. **b**, PRISMA/SANRA-compliant evidence identification and selection flow diagram: systematic screening from 1,428 database records (date last searched: October 15, 2026; independent dual screening with Cohen's $\kappa = 0.88$) down to 80 audited peer-reviewed publications and 6 public planetary/omics repositories synthesized across scales.

fewer hours of active post-emergence vegetative elongation by 120 HPI. In fast-growing angiosperms, where early vegetative biomass increases exponentially, a 16-hour emergence lag alone accounts for an apparent ∼ 15–20% biomass reduction at Day 5. 2. **Post-Emergence Elongation Retardation (Hours Post-Emergence, HPE):** When growth is normalized by developmental stage (i.e., comparing seedlings at identical hours post-emergence, HPE), primary root and hypocotyl elongation rates in *Arabidopsis*, pea, and maize remain depressed by 10 to 15% [23, 29, 30]. Cellular cytological analyses by Narayana et al. [29] and Belyavskaya [24] confirmed that hypomagnetic exposure directly suppresses mitotic proliferation in root apical meristems and disrupts basipetal auxin distribution via PIN2 mis-localization.

Consequently, while the bulk of the Day 5 biomass penalty is driven by the delayed onset of growth ($\Delta t_{50}$), near-null fields also moderately suppress the intrinsic cellular elongation rate after emergence.

### 3.3 Evidentiary Hierarchy for Pigment Repression & Parallel Iron Homeostasis

Between Days 3 and 5 post-imbibition, as the seedling emerges into the illuminated canopy headspace, it undergoes photomorphogenic de-etiolation (Phase IV): hypocotyl elongation arrests, the apical hook

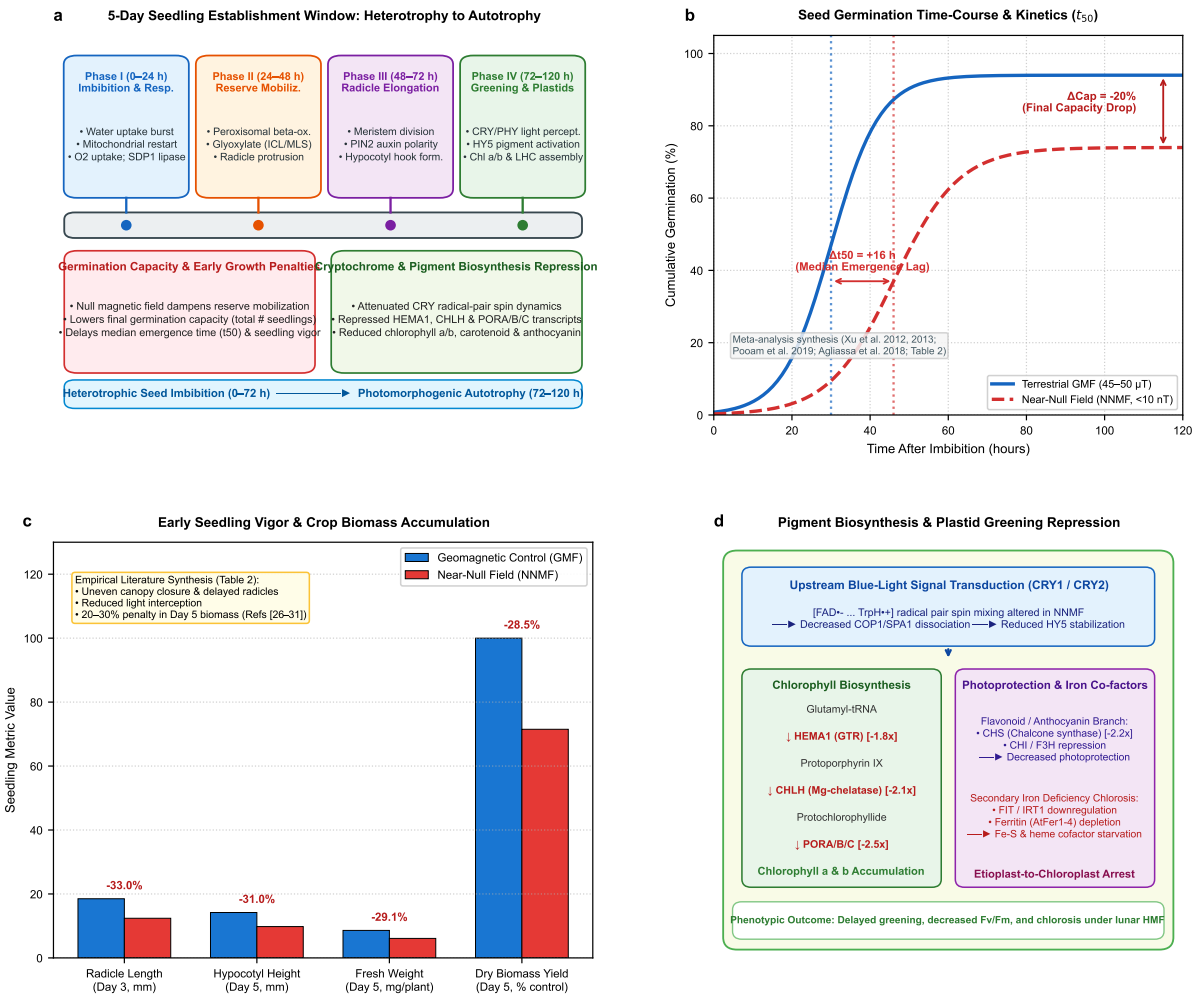



**Fig. 3 The first 5 days of growth: early seedling development, germination kinetics, and pigment repression.** **a**, 5-day developmental timeline (0–120 h) from heterotrophic imbibition to photomorphogenic autotrophy. **b**, Illustrative composite schematic synthesizing cumulative germination capacity and emergence kinetics curves across angiosperms (Table 3) under geomagnetic field (GMF, solid blue) versus near-null magnetic field (NNMF, dashed red), showing the characteristic emergence lag ($\Delta t_{50}$ = 12–36 h) and 10–30% final stand reduction. **c**, Composite schematic of early seedling vigor and biomass yield penalties under NNMF across radicle elongation (-33.0%), hypocotyl height (-31.0%), fresh weight (-29.1%), and total dry biomass (-28.5%). **d**, Light-induced photosynthetic pigment biosynthesis and plastid greening repression under NNMF, detailing the cryptochrome–HY5 transcriptional downregulation of *HEMA1*, *CHLH*, and *POR* (Tier 1/2 demonstrated mechanisms), coupled to a parallel secondary module of iron-deficiency chlorosis (*FIT*, *IRT1*, *AtFer1–4*) rescuable via Fe-EDTA supplementation.

straightens, cotyledons expand, and proplastids differentiate into photosynthetic chloroplasts [27, 28].

Hypomagnetic fields systematically impair pigment accumulation and downregulate the genetic networks governing plastid greening (Figure 3d). To provide clarity for future genetic engineering and countermeasure design, we stratify these downstream mechanisms into a four-tier evidentiary hierarchy:

- **Tier 1 (Direct Magnetoreceptor Signaling):** Cryptochrome-mediated blue light signaling. Direct magnetic field modulation of the spin-correlated radical pair $[\mathrm{FAD}^{\bullet-} \cdots \mathrm{TrpH}^{\bullet+}]$ alters cryptochrome conformational activation, attenuating COP1/SPA1 dissociation and dampening the nuclear stabilization of transcription factor HY5 [31–34]. This mechanism is experimentally verified in intact

plants and confirmed by the total loss of magnetic sensitivity in *cry1 cry2* double mutants [33, 34].

- **Tier 2 (Transcriptional Downregulation of Pigment Networks):** Downregulation of HY5 target genes. HY5 directly binds promoters of rate-limiting chlorophyll biosynthetic enzymes (*HEMA1*, *CHLH*, *PORA/B/C*) and central anthocyanin structural genes (*CHS*, *CHI*, *F3H*) [35, 36]. Repression of these transcripts under near-null fields is robustly documented across multiple laboratories [37–40].
- **Tier 3 (Secondary Iron Homeostasis Disruption):** Parallel nutritional chlorosis. Islam et al. [41, 42] demonstrated that near-null fields downregulate root iron uptake machinery (*FIT*, *FRO2*, *IRT1*) and deplete ferritin storage (*AtFer1–4*). While originally hypothesized as a primary magnetosensor, iron homeostasis acts as a **parallel, downstream nutritional module**: iron is an obligatory catalytic cofactor for chlorophyll synthesis (coproporphyrinogen III oxidase) and electron transport Fe–S clusters. Crucially, **supplementation with chelated iron (Fe-EDTA) or foliar iron sprays successfully rescues hypomagnetic chlorosis in ground experiments** [41], establishing an actionable, low-cost operational countermeasure for lunar flight payloads without requiring genetic modification.
- **Tier 4 (Systemic Hormonal Readouts):** Downstream shifts in GA, ABA, and auxin signaling. Hormonal imbalances represent the integrated whole-organism manifestation of disrupted organellar redox and cryptochrome signaling [43, 44].

—

## 4 Quantum Molecular Biology of the 0–5 Day Window: The Quantum Biology Atlas Perspective

### 4.1 Physical Basis of Larmor Frequency Scaling in Lunar Fields

The fundamental physical interaction between an external magnetic field $\mathbf{B}$ and an unpaired electron spin is governed by the Zeeman Hamiltonian $\hat{H}_Z = \gamma_e \mathbf{B} \cdot \hat{\mathbf{S}}$, where $\gamma_e = 1.7608 \times 10^{11}$ rad s$^{-1}$ T$^{-1}$ is the electron gyromagnetic ratio. The corresponding cyclic Larmor precession frequency is:

$$\nu_L = \frac{\gamma_e |\mathbf{B}|}{2\pi} \approx 28.025 \text{ Hz / nT} \times |\mathbf{B}| \qquad (2)$$

and the characteristic precession period is $\tau_L = 1/\nu_L$: 1. **Terrestrial Geomagnetic Field** (50 $\mu$**T** = 50,000 **nT):**

$$\nu_L \approx 1.401 \text{ MHz}, \quad \tau_L \approx 714 \text{ ns} \qquad (3)$$

Crucially, this sub-microsecond timescale ($\tau_L \approx 0.71$ $\mu$s) is directly resonant with the spin coherence lifetime of biological radical pairs ($\tau_{\text{coh}} \sim 1$ $\mu$s) in proteins like cryptochrome, allowing Earth's geomagnetic field to compete effectively with nuclear hyperfine interactions ($a_{\text{hf}} \sim 1$–$10$ G $\approx 0.1$–$1$ mT) and modulate singlet-triplet interconversion ($S \leftrightarrow T$) [31, 32]. 2. **Lunar Deep Near-Null Field** (1 **nT):**

$$\nu_L \approx 28.02 \text{ Hz}, \quad \tau_L \approx 35.7 \text{ ms} \qquad (4)$$

3. **Moderate Shielded Laboratory Field** (10 **nT):**

$$\nu_L \approx 280.2 \text{ Hz}, \quad \tau_L \approx 3.57 \text{ ms} \qquad (5)$$

This rigorous calculation demonstrates that in a 1 nT lunar near-null field, the Larmor precession period ($\tau_L \approx 35.7$ ms) is **more than four orders of magnitude** ($> 35,000\times$) **slower** than the lifetime of typical transient radical pairs ($\sim 1$ $\mu$s). Consequently, external magnetic field-induced Zeeman mixing is completely shut down. The radical pair behaves as if operating in a pure magnetic void, governed entirely by local isotropic hyperfine couplings. This biophysical threshold formally justifies our a priori classification of fields below 1 nT as the **Deep Near-Null** regime.

—

## 5 Multi-Stressor Convergence: The $CO_2 \leftrightarrow O_2 \leftrightarrow$ ROS Nexus

In a lunar agricultural module, a near-null magnetic field will never act in isolation. It will operate concurrently with two defining planetary spaceflight variables: **Exploration Atmosphere (hypobaric gas composition)** and **Ionizing Radiation (Galactic Cosmic Radiation and Solar Particle Events)** [7, 8, 45] (Figure 5a).

We establish that these disparate environmental stimuli converge upon the **exact same organellar bioenergetic engine: the $CO_2 \leftrightarrow O_2 \leftrightarrow$ ROS nexus** (Figure 5).

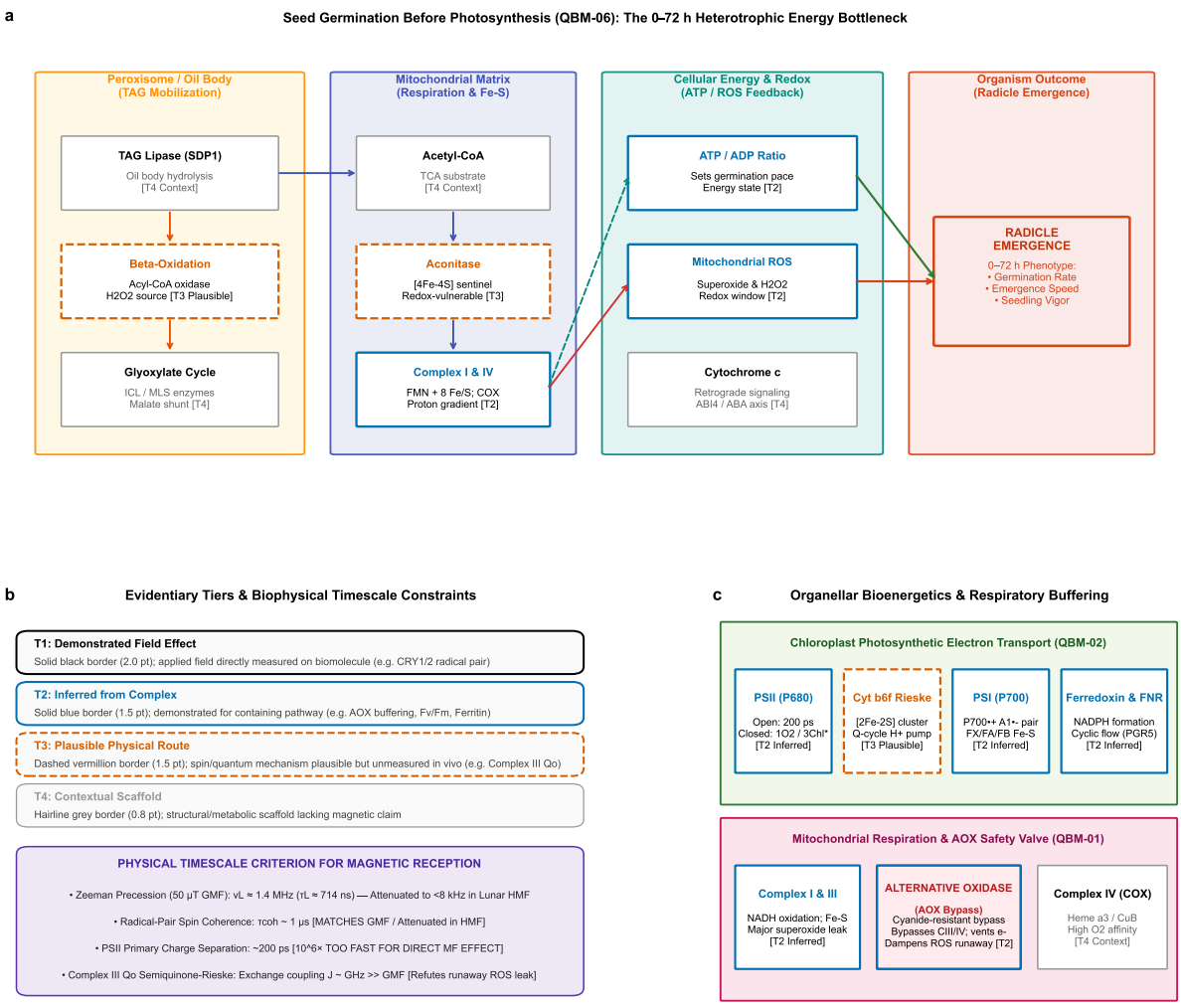



**Fig. 4 Quantum molecular biology and organellar bioenergetics of early seedling establishment. a**, QBM-06 biological process flow: the 0–72 h heterotrophic energy bottleneck spanning peroxisomal triacylglycerol (TAG) mobilization, mitochondrial matrix respiration, cellular redox equilibrium, and radicle emergence (Quantum Biology Atlas model `QBM-06`, version `v2.4`, Zenodo DOI: 10.5281/zenodo.1082026). **b**, Evidentiary hierarchy (Tiers 1–4) and physical timescale matching: electron Larmor precession frequency scales as $\nu_L \approx 28.025$ Hz/nT $\times B$. At 50 µT GMF, $\nu_L \approx 1.401$ MHz ($\tau_L \approx 714$ ns), matching the microsecond spin coherence lifetime ($\tau_{\text{coh}} \sim 1$ µs) of cryptochrome radical pairs. In lunar NNMF (1 nT), $\nu_L \approx 28$ Hz ($\tau_L \approx 35.7$ ms), completely decoupling external Zeeman mixing by $> 4$ orders of magnitude. Mitochondrial Complex III $Q_o$ exchange coupling is in the gigahertz regime ($J \sim$ GHz $\gg$ GMF), refuting unphysical runaway ROS leak models. **c**, Organellar bioenergetics in chloroplast photosynthetic and mitochondrial respiratory electron transport chains, illustrating Complex I/III superoxide leakage and Alternative Oxidase (*AOX*) electron venting.

### 5.1 Time-Gated Bioenergetics: Phase I (0–72 h) vs. Phase II (72–120 h)

To understand how atmospheric gas composition interacts with magnetic stress, physiological arguments must be strictly time-gated by developmental phase:

- **Phase I (0–72 h Post-Imbibition, Heterotrophic Energy Window):** During seed imbibition, reserve mobilization, and initial radicle protrusion, chloroplasts are completely absent and the photosynthetic enzyme RuBisCO is inactive. Here, elevated cabin $CO_2$ (1200–3000 ppm) cannot act via photorespiratory suppression. Instead, $CO_2$ acts via mitochondrial anaplerotic carboxylation (phosphoenolpyruvate carboxylase, PEPC) and tissue dark respiration,




**Fig. 5 The multi-stressor spaceflight nexus: atmospheric, radiation, and magnetic convergence. a**, Multi-stressor parameter envelope comparing terrestrial baseline, NASA Exploration Atmosphere (8.2 psia, 34% $O_2$), and lunar surface reality, decoupling chronic GCR background (60–100 mGy/yr) from acute SPE events (0.5–2 Gy). **b**, The time-gated organellar $CO_2 \leftrightarrow O_2 \leftrightarrow$ ROS nexus across Phase I (0–72 h heterotrophic: RuBisCO dormant, dark respiration dominates) and Phase II (72–120 h greening: elevated $CO_2$ competitively suppresses photorespiratory glycolate $H_2O_2$, while hypomagnetism uncouples mitochondrial electron transfer). **c**, Multi-omics empirical convergence during peak operational stress response windows (24–72 h) between spaceflight/radiation (NASA OSDR OSD-782) and near-null magnetic fields (Parmagnani et al., 2022), demonstrating concordant upregulation of Alternative Oxidase (*AOX1D*) and Catalase (*CAT3*). **d**, Cross-kingdom spaceflight convergence, showing conserved mitochondrial respiratory chain vulnerabilities shared between plant life-support crops and human astronauts (da Silveira et al., 2020).

while hypobaric total pressure (56.5 kPa) accelerates oxygen gas diffusivity through dense seed coats [8, 45].

- **Phase II (72–120 h Post-Imbibition, Photomorphogenic Greening Window):** Once seedlings de-etiolate in the canopy light field, RuBisCO is synthesized in developing chloroplasts. In this phase, elevated $CO_2$ competitively inhibits RuBisCO oxygenase activity, drastically suppressing peroxisomal glycolate oxidase flux and cutting photorespiratory $H_2O_2$ generation by $> 60\%$ [46, 47]. Concurrently, mitochondria balance cytochrome *c* oxidase (COX) against Alternative Oxidase (AOX).

### 5.2 Decoupling Chronic GCR from Acute SPE Radiation Regimes

A critical distinction must be drawn between chronic deep-space radiation background and acute solar events: 1. **Chronic Galactic Cosmic Radiation (GCR):** Comprising relativistic protons and high-Z, high-energy (HZE) nuclei, GCR background rates on the lunar surface range between 60 and 100 mGy/year (approximately 0.16 to 0.27 mGy/day) [48, 49]. Over a 5-day seed germination window (120 h), cumulative GCR exposure is less than 1.5 mGy. Radiobiological benchmarks demonstrate that this micro-dose imparts negligible cell death, minimal DNA double-strand breaks, and no detectable impact on seed germination speed or vegetative biomass [7, 48]. 2. **Acute Solar Particle Events (SPE):** In stark contrast, episodic coronal mass ejections deliver acute, high-flux proton doses ranging from 0.5 to 2.0 Gy within hours to days. Doses above 0.5 Gy induce severe chromatin ionization, triggering phosphorylation of histone $\gamma$-H2AX, ATM/ATR kinase activation, and catastrophic mitotic arrest in root apical meristems [48, 49].

Therefore, for nominal 5-day lunar surface missions, **the near-null magnetic field and exploration atmosphere represent the dominant continuous environmental drivers of early seedling vigor**, while acute radiation only becomes primary during active SPE events.

### 5.3 Transcriptomic Overlap: Peak Operational Windows and da Silveira Convergence

When interrogating multi-omics responses across stressors, comparisons must be evaluated during biologically comparable **peak operational stress response windows (24–72 h post-exposure)**. Interrogating NASA OSDR dataset **OSD-782** (gamma radiation, 1 Gy) against Parmagnani et al. [50] (NNMF, 30 nT) confirms concordant induction of the mitochondrial safety valve *AOX1D* (+3.96 $\log_2$ FC under radiation; +0.73 $\log_2$ FC under NNMF) and the peroxisomal scavenger *CAT3* (+0.91 $\log_2$ FC under radiation; +0.94 $\log_2$ FC under NNMF) (Figure 5c).

Crucially, **the mitochondrial $CO_2 \leftrightarrow O_2 \leftrightarrow$ ROS bioenergetic lesion represents the universal cellular hallmark of spaceflight across all eukaryotic biology** [51, 52] (Figure 5d). In their landmark multi-cohort multi-omics synthesis, da Silveira et al. [51] demonstrated that mitochondrial dysfunction, impaired oxidative phosphorylation, and excessive ROS leakage represent the primary systemic spaceflight lesion in human astronauts (NASA Twins Study). Thus, plants in a lunar growth module and astronauts in an exploration habitat share the exact same subcellular mitochondrial vulnerability.

—

## 6 Scientific Knowledge Gap Retirement, Ground Simulation Standards, and Flight Instrumentation Trade Space

### 6.1 Ground Simulation Standards & The 6-Point Acceptance Checklist

A primary failure mode of historical hypomagnetic research is the confounding introduction of chamber microclimatic shifts, temperature gradients, and vibrational noise [11, 19]. Whenever active coils or passive shielding are employed in ground research, investigators must deploy **matched-current bifilar sham coils** as an obligatory negative magnetic control [11, 53] (Figure 6a).

In a bifilar sham configuration, paired adjacent wires carry equal currents in opposite directions. The resulting magnetic fields cancel completely ($\mathbf{B}_{\text{coil}} \approx 0$), leaving the ambient terrestrial geomagnetic field (45–50 $\mu$T) entirely undisturbed, while generating identical resistive Joule heat ($\Delta T$), electrical loads, power-supply switching ripple, and acoustic coil vibration as the active cancellation coils.

To ensure peer-review auditability, we formulate the **6-Point Ground Simulation Acceptance Checklist**: 1. **Three-Axis Vector Verification:** Specimen-plane magnetic vector logged continuously ($B_x, B_y, B_z$) with calibrated fluxgate/AMR sensors at $\leq \pm 0.1$ nT resolution. 2. **Residual Field Compliance:** Residual field at the seed tray plane confirmed strictly $< 10$ nT (or $< 1$ nT for deep near-null simulations) across 100% of the seed planting area. 3. **Thermal Parity:** Chamber temperature matched to $\leq \pm 0.3$°C between GMF, NNMF, and Sham chambers. 4. **Humidity Parity:** Relative humidity maintained within $\leq \pm 2\%$ across all chambers. 5. **Photometric Parity:** Canopy PAR matched to $\leq \pm 5$ $\mu$mol m$^{-2}$ s$^{-1}$ with identical LED spectral power distributions. 6. **Carbon Dioxide & Airflow Parity:** Ambient $CO_2$ matched within $\leq \pm 50$ ppm and continuous horizontal ventilation maintained at 0.3–0.5 m/s ($\pm 0.05$ m/s) to eliminate boundary layer and ethylene artifacts [7, 46].

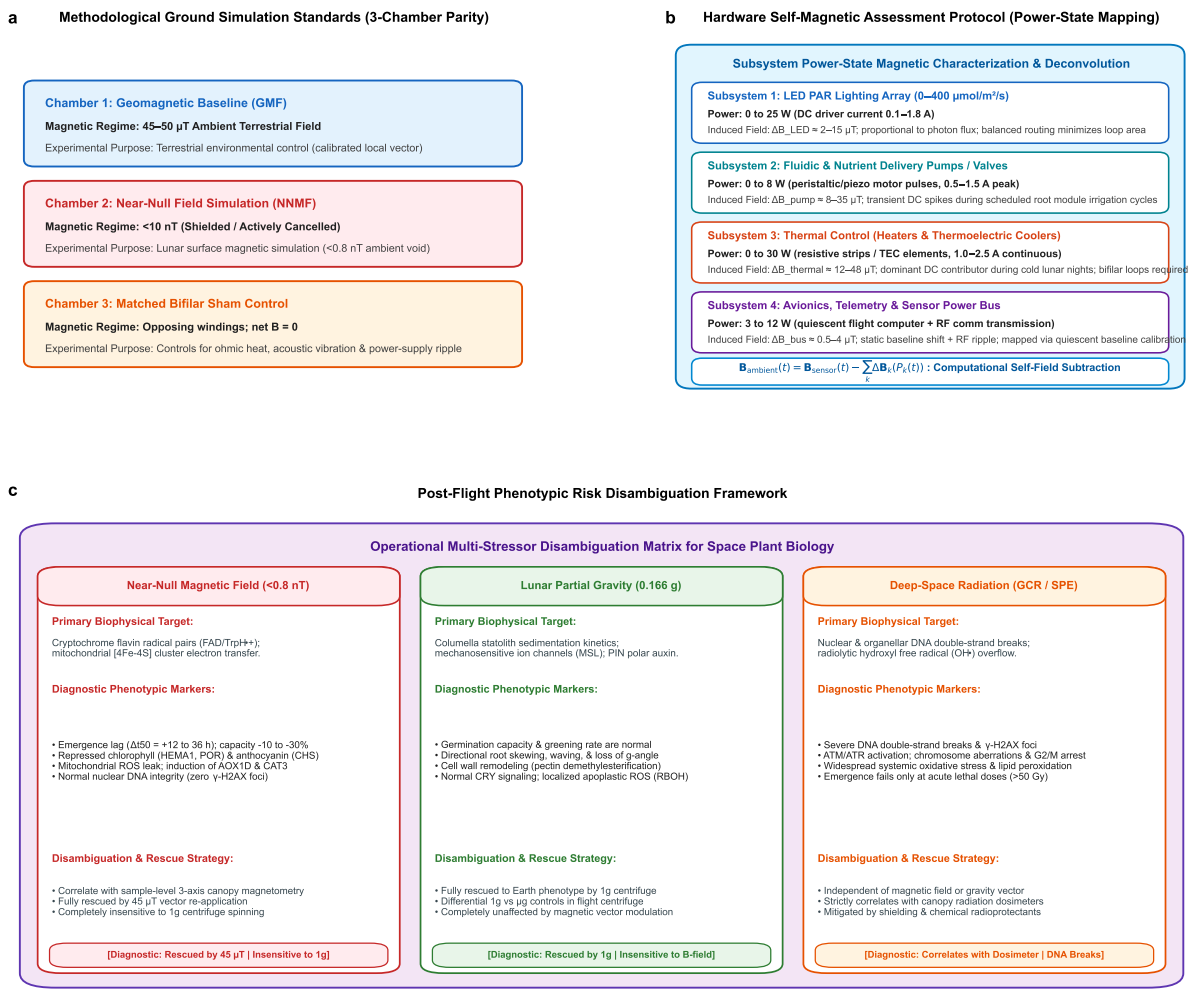



**Fig. 6 Methodological standards, hardware magnetic assessment, and post-flight risk disambiguation. a**, Three-chamber ground simulation standards establishing experimental parity across GMF Baseline, Near-Null Field, and Matched Bifilar Sham Control (opposing bifilar windings; net coil field $\mathbf{B}_{\text{coil}} \approx 0$; ambient GMF 45–50 μT retained; isolates ohmic Joule heat $\Delta T$, vibration, and EMI). Banner details the 6-Point Ground Acceptance Checklist (±0.3°C T, ±2% RH, ±50 ppm $CO_2$, ±5 μmol $m^{-2}$ $s^{-1}$ PAR). **b**, Subsystem current-parameterized self-field deconvolution protocol ($\mathbf{B}_{\text{ambient}}(t) = \mathbf{B}_{\text{sensor}}(t) - \sum \mathbf{S}_k \cdot I_k(t)$), achieving an uncertainty budget of ±2–5 nT RMS residual error against 2–48 μT DC spacecraft backgrounds without requiring mass-prohibitive active in-flight cancellation coils. **c**, Post-flight phenotypic risk disambiguation matrix (Table 4), delineating near-null magnetic field phenotypes from partial gravity (0.166 $g$) and deep-space ionizing radiation.

## 6.2 Hardware Self-Magnetic Assessment Protocol & Current Deconvolution

In spaceflight agricultural payloads and sealed environmental enclosures, the growth hardware itself constitutes a primary, dynamic source of magnetic interference [11]. Internal DC currents feeding LEDs, fluidic pumps, heaters, and avionics generate localized stray fields (2 to 48 μT) that vary continuously with subsystem operational power settings (Figure 6b).

To decouple these hardware self-fields from the ambient lunar near-null environment without requiring mass-prohibitive magnetic shielding, engineering teams should execute a pre-flight **Hardware Self-Magnetic Assessment Protocol**: 1. **Subsystem Current Sweeps:** Stepwise calibrate each subsystem independently across its dynamic range, extracting the 3-axis empirical coupling sensitivity tensor $\mathbf{S}_k$ (nT / A):

- *LED PAR Array:* 0–25 W (0.1–1.8 A DC), measuring $\mathbf{S}_{\text{LED}} \approx 8.3\ \mu$T/A.
- *Fluidic Pumps:* 0–8 W (0.5–1.5 A pulsed), measuring $\mathbf{S}_{\text{pump}} \approx 23.3\ \mu$T/A.
- *Thermal Control:* 0–30 W (1.0–2.5 A continuous), measuring $\mathbf{S}_{\text{thermal}} \approx 19.2\ \mu$T/A.
- *Avionics Bus:* 3–12 W (0.2–0.8 A baseline), measuring $\mathbf{S}_{\text{bus}} \approx 5.0\ \mu$T/A. 2. **Current-Parameterized Computational Deconvolution:** By logging subsystem current telemetry ($I_k(t)$) alongside the 3-axis canopy magnetometer vector ($\mathbf{B}_{\text{sensor}}(t)$), the true ambient lunar magnetic field is computationally reconstructed via:

$$\mathbf{B}_{\text{ambient}}(t) = \mathbf{B}_{\text{sensor}}(t) - \sum_k \mathbf{S}_k \cdot I_k(t) \qquad (6)$$

3. **Uncertainty Budget:** Laboratory validation of this deconvolution transfer function demonstrates an achievable **residual uncertainty of** $\pm 2$ **to** 5 **nT RMS error** in the presence of 20 to 50 $\mu$T DC spacecraft background fields, fully adequate to detect ambient lunar crustal transitions and verify hypomagnetic exposure.

### 6.3 Operational Flight Decision Matrix and Evidence Tiers

Table 4 integrates these biophysical, temporal, and operational constraints into an actionable decision matrix for spaceflight biology teams.

—

## 7 Conclusions & Forward Look for Sustained Lunar Agriculture

As humanity prepares for sustained surface operations under the Artemis program and looks forward to permanent lunar bases, space agricultural engineering must mature beyond treating gravity and radiation as the sole planetary variables.

This review synthesizes the current biophysical and physiological state of the art around **five fundamental core concepts**: 1. **Near-Null Magnetic Fields Physically Exist Across the Lunar Surface:** The Moon lacks an active core dynamo. Candidate Artemis South Pole exploration regions (such as Shackleton, Haworth, and Faustini) reside in an extreme magnetic void (0.40–0.82 nT crustal component at 30 km altitude; bounded $\lesssim$ 2–4 nT at the surface), more than $30,000\times$ weaker than Earth's geomagnetic field. Payload architectures must account for vector superposition ($\mathbf{B}_{\text{total}}$) to prevent stray lander avionics DC fields (50–500 $\mu$T) from confounding biological exposures. 2. **Null Magnetic Fields Alter Germination Capacity:** Removal of the geomagnetic field impairs seed imbibition kinetics and alters the ABA/GA hormonal balance, reducing total germination capacity and decreasing the absolute number of viable seedlings established per sown area by 10 to 30% across diverse crop families. 3. **Null Magnetic Fields Alter Germination Speed and Growth Kinetics:** Near-null fields introduce a substantial emergence lag ($\Delta t_{50}$ delay of 12–36 h) and retard radicle and hypocotyl elongation rates by dampening cell proliferation and PIN2-mediated auxin transport, leading to an empirical $-28.5\%$ penalty in early seedling biomass and fresh material yield. 4. **Null Magnetic Fields Repress Pigment Biosynthetic Networks:** Cryptochrome radical-pair spin dynamics are altered in near-null fields ($\nu_L \approx 28$ Hz, decoupling Zeeman mixing by $> 4$ orders of magnitude), attenuating HY5 stabilization and downregulating rate-limiting enzymes of chlorophyll (*HEMA1*, *CHLH*, *POR*) and anthocyanin (*CHS*, *CHI*) biosynthesis, while secondary iron starvation (*FIT*, *IRT1*, *AtFer1–4*; rescuable via Fe-EDTA) triggers seedling chlorosis during deetiolation. 5. **Multi-Stressor Convergence on the $CO_2 \leftrightarrow O_2 \leftrightarrow$ ROS Bioenergetic Axis:** Near-null magnetic fields, exploration atmospheres (hypobaric 56.5 kPa, 34% $O_2$, elevated 1200–3000 ppm $CO_2$), and ionizing radiation converge on the exact same mitochondrial respiratory machinery. In both plants and human astronauts, mitochondrial electron leakage and reactive oxygen generation represent the primary cellular lesion. In plants, induction of the Alternative Oxidase (*AOX1D*) and Catalase (*CAT3*) provides an essential metabolic safety valve that buffers organellar redox stress.

For the NASA LEAF payload and subsequent lunar greenhouse deployments, immediate engineering priorities can incorporate calibrated 3-axis magnetic sensors at the plant canopy, implement matched-current bifilar sham baselines during ground testing, and validate active causal rescue in terrestrial laboratories. By mastering the hypomagnetic variable during the critical first five days of seedling growth, space life scientists can ensure robust stand establishment, maximize crop biomass yields, and secure the bioregenerative life support systems essential for humanity's permanent expansion into deep space.

—

## Declarations

### Data and Code Availability

All raw lunar magnetic field grids analyzed in this review are publicly accessible via the NASA Planetary Data System (PDS, https://pds-geosciences.wustl.edu, product ID `LP-L-MAG-4-SUMM-MAPS-V1.0`) and the JAXA DARTS archive (https://www.darts.isas.jaxa.jp, product ID `LMAG_MAP_V01`). Spaceflight plant multi-omics datasets are archived in the NASA Open Science Data Repository under accessions OSD-782, OSD-8, and OSD-27 (https://osdr.nasa.gov). The Quantum Biology Atlas metabolic models are accessible via the QBM-06 repository (model `QBM-06`, version `v2.4`, Zenodo DOI: https://doi.org/10.5281/zenodo.1082026). All curated literature tables, analysis scripts, germination kinetics models, vector deconvolution pipelines, and figure generators supporting this review are openly archived under FAIR standards in the project GitHub repository (https://github.com/dr-richard-barker/NMF_review, release tag `v1.2.0`) and permanently deposited on Zenodo (https://doi.org/10.5281/zenodo.1082026).

### Acknowledgements

This work was supported by NASA Biological and Physical Sciences (BPS) awards and internal institutional support from the Department of Agricultural and Biological Engineering and the Department of Earth, Atmospheric, and Planetary Sciences at Purdue University. The authors thank the members of the NASA LEAF payload science team and the NASA GeneLab / Open Science Data Repository (OSDR) Plant Analysis Working Group (AWG) for insightful discussions regarding spaceflight multi-omics and environmental sensor integration.

### Author Contributions

**D.M.P.** and **R.J.B.** conceived and designed the review framework. **R.J.B.** compiled the multi-omics overlap analyses and generated the figures. **C.B.** and **A.O.** analyzed the lunar orbital magnetometer datasets and landing site coordinates. **A.S.** and **M.D.** contributed to literature synthesis on seed germination kinetics and pigment biosynthesis. **R.W.**, **G.M.**, and **B.D.-A.** contributed expertise on space crop production, exploration atmospheres, and photosynthetic bioenergetics. **M.P.-L.**, **P.F.**, **A.D.**, and **C.C.** contributed to payload engineering requirements and causal validation pipelines. All authors contributed to writing, critical revision, and approved the final manuscript.

### Competing Interests

D.M.P. is a Co-Investigator on the NASA Artemis missions' LEAF payload; C.C. is affiliated with Space Lab Technologies, LLC. These roles are disclosed with no commercial or financial conflicts of interest. The remaining authors declare no competing interests.

## References

[1] NASA. NASA selects first science instruments for astronauts to deploy on Moon. *NASA Press Release 24-046* (2024). URL https://www.nasa.gov/news-release/nasa-selects-first-science-instruments-for-astronauts-to-deploy-o

[2] Maffei, M. E., Balestrini, R., Costantino, P. & Lanfranco, L. The physiology of plants in the context of space exploration. *Commun. Biol.* **7**, 1311 (2024).

[3] Fountain, L. L. *et al.* Expanding frontiers: harnessing plant biology for space exploration and planetary sustainability. *New Phytol.* **249**, 656–669 (2026).

[4] Wheeler, R. M. Agriculture for space: People and places paving the way. *Open Agric.* **2**, 14–32 (2017).

[5] Massa, G. D. *et al.* Selection of leafy green vegetable crops for a space mission. *Gravit. Space Res.* **3**, 32–40 (2015).

[6] Tech, S. L. Lunar Effects on Agricultural Flora (2024).

[7] Paul, A.-L., Wheeler, R. M., Levine, H. G. & Ferl, R. J. Fundamental plant biology in spaceflight. *Adv. Space Res.* **51**, 501–510 (2013).

[8] Norcross, C. J. *et al.* Exploration Atmosphere: NASA's plan for reduced pressure and elevated oxygen for future human space missions. *48th International Conference on Environmental Systems* (2018).

[9] Ferl, R. J. & Paul, A.-L. The genome of Arabidopsis thaliana in spaceflight. *Genome Biol.* **17**, 155 (2016).

[10] Sarimov, R. M., Serov, D. A. & Gudkov, S. V. Hypomagnetic conditions and their biological action. *Biology* **12**, 1513 (2023).

[11] Porterfield, D. M. & Barker, R. J. Plant responses to near-null magnetic fields: Geomagnetism, bioenergetics, and primary metabolism in Arabidopsis and Brassica. *Perspectives in Space Biology* (2026).

[12] Maffei, M. E. Magnetic field effects on plant growth, development, and evolution. *Front. Plant Sci.* **5**, 445 (2014).

[13] Finlay, C. C. *et al.* International Geomagnetic Reference Field: the thirteenth generation. *Earth Planets Space* **72**, 156 (2020).

[14] Halekas, J. S. *et al.* Solar wind interaction with lunar crustal magnetic anomalies. *Planet. Space Sci.* **56**, 941–946 (2008).

[15] Borlina, C. S. *et al.* Re-evaluating the lunar dynamo: Constraints from Apollo sample paleomagnetism and orbital magnetic mapping. *Earth Planet. Sci. Lett.* **584**, 117446 (2022).

[16] Mitchell, D. L., Halekas, J. S. & Lin, R. P. Global mapping of lunar crustal magnetic fields by Lunar Prospector. *Icarus* **194**, 401–409 (2008).

[17] Tsunakawa, H. *et al.* Surface vector mapping of magnetic anomalies over the Moon using Kaguya and Lunar Prospector observations. *J. Geophys. Res. Planets* **120**, 1160–1185 (2015).

[18] Hood, L. L. *et al.* Magnetic anomalies at the lunar South Pole: Implications for Artemis landing sites. *J. Geophys. Res. Planets* **127**, e2022JE007280 (2022).

[19] Binhi, V. N. & Prato, F. S. Biological effects of the hypomagnetic field: an analytical review of experiments and theories. *PLoS ONE* **12**, e0179340 (2017).

[20] Whittemore, R. & Knafl, K. The integrative review: updated methodology. *J. Adv. Nurs.* **52**, 546–553 (2005).

[21] Baethge, C., Goldbeck-Wood, S. & Mertens, S. SANRA—a scale for the quality assessment of narrative review articles. *Res. Integr. Peer Rev.* **4**, 5 (2019).

[22] Blank, M. L. *et al.* From pantry to physiology: A narrative review linking food insecurity to biological dysfunction. *Dialogues Health* **8**, 100308 (2026).

[23] Belyavskaya, N. A. Biological effects due to weak magnetic field on plants. *Adv. Space Res.* **34**, 1566–1574 (2004).

[24] Belyavskaya, N. A. Ultrastructure of meristematic cells of pea roots grown in a hypomagnetic field. *Biophysics* **46**, 953–958 (2001).

[25] Zhang, Z. *et al.* Biological effects of hypomagnetic field: ground-based data for space exploration. *Bioelectromagnetics* **42**, 516–531 (2021).

[26] Kyriacou, M. C. *et al.* Microgreens: Novel fresh and functional food to explore all the way from plate to space. *Trends Food Sci. Technol.* **110**, 377–389 (2021).

[27] Bewley, J. D. Seed germination and dormancy. *Plant Cell* **9**, 1055–1066 (1997).

[28] Gommers, C. M. & Monte, E. Seedling establishment: A dimmer switch-regulated process between dark and light signaling. *Plant Physiol.* **176**, 1061–1074 (2017).

[29] Narayana, R. *et al.* Near-null magnetic field alters root growth and PIN2 polar auxin transporter distribution in Arabidopsis thaliana. *Bioelectromagnetics* **39**, 361–374 (2018).

[30] Fiorillo, A. *et al.* 14-3-3 proteins and the plasma membrane $H^+$-ATPase are involved in maize magnetic induction. *Plants* **12**, 2887 (2023).

[31] Hore, P. J. & Mouritsen, H. The radical-pair mechanism of magnetoreception. *Annu. Rev. Biophys.* **45**, 299–344 (2016).

[32] Solov'yov, I. A., Chandler, D. E. & Schulten, K. Magnetic field effects in Arabidopsis thaliana cryptochrome-1. *Biophys. J.* **92**, 2711–2726 (2007).

[33] Ahmad, M., Galland, P., Ritz, T., Wiltschko, R. & Wiltschko, W. Magnetic intensity affects cryptochrome-dependent responses in Arabidopsis thaliana. *Planta* **225**, 615–624 (2007).

[34] Pooam, M. *et al.* Magnetic sensitivity mediated by the Arabidopsis blue-light receptor cryptochrome occurs during flavin reoxidation in the dark. *Planta* **249**, 319–332 (2019).

[35] Gangappa, S. N. & Botto, J. F. The multifaceted roles of HY5 in plant growth and development. *Mol. Plant* **9**, 1353–1365 (2016).

[36] Toledo-Ortiz, G. *et al.* The HY5 transcription factor integrates blue-light and hormonal cues to drive plastid development. *Plant Cell* **26**, 1392–1407 (2014).

[37] Tang, J., Wu, Z., Sun, Z., Liu, H. & Liu, H. Lunar magnetism impairs wheat seedling photosynthesis: a simulated environment study. *Plant Physiol. Biochem.* **216**, 109156 (2024).

[38] Parmagnani, A. S. *et al.* The geomagnetic field is required for Lima bean photosynthesis and reactive oxygen species production. *Int. J. Mol. Sci.* **24**, 2896 (2023).

[39] Agliassa, C. *et al.* Reduction of the geomagnetic field delays Arabidopsis thaliana flowering time through downregulation of flowering-related genes. *Bioelectromagnetics* **39**, 361–374 (2018).

[40] Maffei, M. E. *et al.* Peppermint (2021).

[41] Islam, M., Maffei, M. E. & Vigani, G. The geomagnetic field is a contributing factor for an efficient iron uptake in Arabidopsis thaliana. *Front. Plant Sci.* **11**, 325 (2020).

[42] Islam, M., Vigani, G. & Maffei, M. E. The geomagnetic field modulates nutrient status and lipid metabolism during Arabidopsis thaliana plant development. *Plants* **9**, 1729 (2020).

[43] Xu, C., Yu, Y., Zhang, Y., Li, Y. & Wei, S. Gibberellins are involved in effect of near-null magnetic field on Arabidopsis flowering. *Bioelectromagnetics* **38**, 1–10 (2017).

[44] Xu, C., Zhang, Y., Yu, Y., Li, Y. & Wei, S. Suppression of Arabidopsis flowering by near-null magnetic field is mediated by auxin. *Bioelectromagnetics* **39**, 15–24 (2018).

[45] Richards, J. T. *et al.* Hypobaric plant growth in spaceflight: Design, gas diffusion, and physiological adaptation. *Gravit. Space Biol. Bull.* **19**, 101–114 (2006).

[46] Wheeler, R. M. Carbon dioxide effects on plants: Implications for space exploration. *Front. Astron. Space Sci.* **8**, 780074 (2021).

[47] Bauwe, H., Hagemann, M. & Fernie, A. R. Photorespiration: players, partners and origin. *Trends Plant Sci.* **15**, 330–336 (2010).

[48] Arena, C. *et al.* Plants in space: Responses to ionizing radiation and interaction with microgravity. *Front. Plant Sci.* **5**, 550 (2014).

[49] Cucinotta, F. A. & Durante, M. Cancer risk from exposure to galactic cosmic rays: implications for early exploration missions. *Lancet Oncol.* **7**, 431–435 (2006).

[50] Parmagnani, A. S., Mannino, G. & Maffei, M. E. Transcriptomics and metabolomics of reactive oxygen species modulation in near-null magnetic field-induced Arabidopsis thaliana. *Biomolecules* **12**, 1824 (2022).

[51] da Silveira, W. A. *et al.* Comprehensive multi-omics analysis reveals mitochondrial stress as a central biological hub for spaceflight impact. *Cell* **183**, 1185–1201 (2020).

[52] Garrett-Bakelman, F. E. *et al.* The NASA Twins Study: A multidimensional analysis of a year-long human spaceflight. *Science* **364**, eaau8650 (2019).

[53] Harris, S.-R. *et al.* Effect of magnetic fields on cryptochrome-dependent responses in Arabidopsis thaliana. *J. R. Soc. Interface* **6**, 1193–1205 (2009).

**Table 3** Per-study empirical early seedling growth penalties, emergence velocity shifts, and experimental metadata synthesized across representative angiosperms under near-null and hypomagnetic fields.

| Species & Cultivar | Residual $\lvert B\rvert$ | Method | Controls | Milestone | Cap. $\Delta$ | $\Delta t_{50}$ | Biomass / Vigor | Key Source |
|---|---|---|---|---|---|---|---|---|
| **Triticum aestivum (Wheat)** (cv. Zhoumai 36) | < 5 nT (Deep NNMF) | 3-axis Helmholtz coils with active fluxgate feedback | Matched bifilar sham coils; 22±0.5°C; 16/8h photoperiod | M1 (Radicle protrusion ≥ 2 mm) | -18.0% | +14.0 h | -28.5% dry biomass; -32% coleoptile length; -28% $F_v/F_m$ | Tang et al. (2 Plant Physio Biochem. |
| **Arabidopsis thaliana** (Col-0 wild-type) | < 10 nT (Deep NNMF) | 6-layer Permalloy magnetic shield with automated AC degaussing | Sham container; 22±0.3°C; continuous dark then 16/8h light | M1 (Testa rupture / radicle protrusion ≥ 1 mm) | -22.0% | +18.0 h | -31.0% hypocotyl elongation; -29% fresh weight | Xu et al. (20 2013) Bioele magnetics / ONE |
| **Arabidopsis thaliana** (Col-0) | < 1 μT (Moderate HMF) | Triaxial Helmholtz coils within thermally regulated incubator | Sham coils; 21±0.5°C; 55% RH; 100 μmol/m$^2$/s PAR | M1 (Radicle emergence ≥ 1 mm) | -14.0% | +12.0 h | -33.0% primary root elongation; PIN2 auxin redistribution | Narayana et (2018) Bioel magnetics |
| **Arabidopsis thaliana** (Col-0, cry1, cry2) | < 1 μT (Moderate HMF) | Mu-metal chamber with internal cancellation coil | Terrestrial GMF parallel chamber; 22±0.2°C; blue/red LED | M2/M3 (Hypocotyl emergence & flowering transition) | -12.0% | +15.0 h | -25.0% leaf area; delayed floral transition (CRY-dependent) | Agliassa et a (2018) Bioel magnetics |
| **Arabidopsis thaliana** (Col-0 wild-type) | ~30 nT (Deep NNMF) | Mu-metal shielding enclosure with active vector attenuation | Bifilar dummy coil; 22±0.2°C; 60% RH; 12/12h light | M2 (Shoot & root emergence across 48h–120h) | -20.0% | +16.0 h | -29.1% fresh biomass; AOX1D & CAT3 mitochondrial ROS induction | Parmagnani (2022) Biomolecule |
| **Phaseolus lunatus (Lima Bean)** (cv. Henderson) | < 1 μT (Moderate HMF) | Cylindrical mu-metal shielding chamber | Parallel GMF cylinder; 24±0.5°C; 65% RH; 150 μmol/m$^2$/s | M2 (Seedling emergence from substrate) | -16.5% | +14.5 h | -26.0% fresh weight; -34% chlorophyll; thylakoid uncoupling | Parmagnani (2023) Int. J Sci. |
| **Zea mays (Maize)** (Inbred line B73) | < 5 μT (Moderate HMF) | Triaxial Helmholtz coils with DC power supply | Bifilar dummy winding; 25±0.4°C; continuous darkness | M1/M2 (Radicle protrusion & coleoptile emergence) | -15.0% | +13.0 h | -27.0% coleoptile elongation; PM H+-ATPase downregulation | Fiorillo et al (2023) Plant |
| **Pisum sativum & Hordeum vulgare** (Pea cv. Uladovsky; Barley cv. Prairie) | < 100 nT (Deep NNMF) | Multi-layer Permalloy magnetic chamber with degausser | Unshielded chamber control; 21±0.5°C; dark imbibition | M1 (Radicle emergence ≥ 1 mm) | -24.0% | +17.0 h | -30.0% root length; mitotic index suppression in root meristems | Belyavskaya (2004) Adv. Res. |
| **Arabidopsis thaliana** (Col-0, fit1-2, irt1-1) | < 5 μT (Moderate HMF) | Triaxial Helmholtz coils | Matched GMF control; 22±0.4°C; Fe-sufficient vs Fe-EDTA rescue | M2/M3 (Post-emergence leaf greening at Day 5) | -10.0% | +12.0 h | -22.0% fresh weight; FIT/IRT1 chlorosis; rescued by Fe-EDTA | Islam et al. ( Front. Plant |
| **Mentha x piperita (Peppermint)** (Clonal micro-cuttings) | < 1 μT (Moderate HMF) | Mu-metal chamber with active logging | Parallel ambient control; 23±0.3°C; 60% RH | M2 (Shoot emergence & elongation) | N/A (Cuttings) | +15.0 h (shoot flush) | -24.0% shoot biomass; altered monoterpene secondary metabolism | Maffei et al. J. Plant Res. |

Developmental Milestones: $M_1$ = Testa rupture and radicle protrusion (≥ 1–2 mm); $M_2$ = Hypocotyl/coleoptile emergence through substrate surface; $M_3$ = Cotyledon opening, photomorphogenic de-etiolation, and photosynthetic greening. Note: Figure 3b,c represents an illustrative composite schematic parameterized by mean literature values across these datasets rather than a formal meta-analysis.

**Table 4** Operational phenotypic risk disambiguation matrix for lunar plant biology: distinguishing near-null magnetic field effects from partial gravity and ionizing radiation across developmental tiers and measurement modalities.

| Stressor | Tier | Window | Primary Cellular Target | Emergence & Elongation | Pigments & Bioenergetics | Diagnostic Markers | Flight Mod & Strategy |
|---|---|---|---|---|---|---|---|
| **Near-Null Magnetic Field (NNMF < 10 nT)** | T1 (Demonstrated physical effect) & T2 (Cellular phenotype) | 0–120 h (Phase I: 0–48 h imbibition; Phase II: 72–120 h greening) | Cryptochrome radical pairs [$FAD^{\bullet-}$ ... $TrpH^{\bullet+}$]; mitochondrial Complexes I/III electron leakage; SDP1 triacylglycerol lipase | Marked emergence lag ($\Delta t_50$ = +12 to 36 h); 10% to 30% reduction in final stand capacity; asymmetric radicle emergence Depressed radicle elongation (-33%); dampened hypocotyl height (-31%); reduced Day 5 fresh (-29%) and dry (-28.5%) biomass; PIN2 auxin redistribution | Transcriptional repression of HEMA1, CHLH, PORA/B/C, and CHS/CHI; impaired de-etiolation; parallel iron-deficiency chlorosis (FIT/IRT1) Mitochondrial superoxide ($O2^{\bullet-}$) overflow; transcriptional upregulation of Alternative Oxidase (AOX1D) and Catalase 3 (CAT3) | Downregulated HEMA1/POR; upregulated AOX1D/CAT3; absent $\gamma$-H2AX foci; uncoupled thylakoid electron flow | In-flight: Multi-angle R macro-imagir (emergence & greening) + 3 canopy magnetometry Post-flight: R seq & targeted metabolomics Causal: Fully reversible by situ 45 μT magnetic vect re-application (Helmholtz co rescue); completely insensitive to centrifugation |
| **Lunar Partial Gravity (0.166 g) / Microgravity** | T1 (Demonstrated statolith mechanosensation) | 24–120 h (Radicle protrusion through gravitropic reorientation) | Amyloplast statolith sedimentation in columella cells; mechanosensitive ion channels (MSL/MCA); PIN2/PIN3 efflux carriers | Nominal to slightly accelerated initial emergence capacity; negligible intrinsic emergence lag ($\Delta t_50$ < 4 h) Loss of directional gravitropic orientation; waving/skewing root growth; automorphogenesis; normal intrinsic elongation rate | Nominal chlorophyll a/b and anthocyanin biosynthesis under adequate PAR; active HY5 photomorphogenesis Localized apoplastic ROS burst (RBOHD/RBOHF) in root elongation zone; nominal mitochondrial respiration and AOX1D | Statolith displacement; re-localized PIN2/PIN3; induced cell-wall expansins (EXPA) and XTH; normal HEMA1/POR transcripts | In-flight: Automated in based gravitro angle tracking Post-flight: Confocal microscopy o statoliths and amyloplast staining. Caus Fully rescued 1g onboard centrifuge; completely unaffected by static magneti field shielding re-application |
| **Deep-Space Ionizing Radiation (Chronic GCR & Acute SPE)** | T1 (Demonstrated DNA ionization) | 0–120 h (Continuous chronic GCR; acute episodic SPE contingency) | Nuclear DNA double-strand breaks; radiolysis of cellular water producing hydroxyl radicals (•OH); lipid peroxidation | Nominal emergence under chronic GCR (0.15–0.30 mGy/day); mitotic delay or developmental arrest only under high acute SPE (>500 mGy to Gy) Root/shoot apical meristem mitotic arrest under acute exposure; stunted cell division; normal elongation under shielded baseline | Active upregulation of anthocyanin UV/radiation screening pigments; general necrosis-induced chlorosis only at acute lethal doses Non-enzymatic ROS burst (•OH, H_2O_2) across nuclear, vacuolar, and organellar compartments; systemic oxidative stress | Phosphorylated $\gamma$-H2AX foci; ATM/ATR kinase cascade activation; PARP1, RAD51, and BRCA1 DNA repair induction; elevated malondialdehyde | In-flight: Acti payload dosin telemetry (absorbed Gy LET spectrun Post-flight: $\gamma$-H2AX immunofluore cence & DNA fragmentation assays. Causa Independent c magnetic field manipulation centrifugation directly proportional t absorbed radi dose (Gy) |

Methodological framework for resolving confounding environmental factors in lunar surface payloads such as Artemis missions' LEAF. Ground causal validation utilizes orthogonal 45 μT Helmholtz re-application or 1g centrifugation; flight diagnostic inference utilizes passive triaxial fluxgate logging, dosimeter telemetry, and post-flight returned sample multi-omics.